Journal of Sound and Vibration 468 (2020) 115085

Contents lists available at ScienceDirect

Journal of Sound and Vibration

journal homepage: www.elsevier.com/locate/jsvi

Numerical analysis of sound radiation from rotating discs

M. Maeder [a,*], R. D'Auria [a,b], E. Grasso [a,b], G. Petrone [b], S. De Rosa [b], M. Klaerner [c], L. Kroll [c], S. Marburg [a]

[a] Technical University of Munich, Munich, Germany
[b] Università degli Studi di Napoli "Federico II", Napoli, Italy
[c] Chemnitz University of Technology, Chemnitz, Germany

ARTICLE INFO

Article history:
Received 22 August 2019
Revised 9 November 2019
Accepted 12 November 2019
Available online 18 November 2019
Handling Editor: A. Tsouvalas

Keywords:
FEM
BEM
Rotating disc
Sound radiation
Mode splitting
Lumped parameter model

ABSTRACT

The analysis of sound radiation from rotating elastic discs, e.g. saw blades, is an interesting research topic. Especially for people who work in the vicinity of such machines, health related issues with respect to noise exposure levels gain more and more awareness. Therefore, the industry is faced with the challenge of developing quieter products in order to improve the working environment and to extend the time a worker can use these tools before a harmful situation arises. Moreover, less noise emission means less energy consumption and therefore a higher productivity. In this paper, the authors investigate the sound radiation from a rotating disc where the sound power is used as a global measure for the acoustic performance. Different methods for calculating the sound power of a spinning saw blade are compared. These are a fully coupled finite element approach, a hybrid finite element/boundary element approach, a simplified form of the RAYLEIGH integral known as the lumped parameter model, and the equivalent radiated sound power. The results show good agreement between the costly full models and those utilizing approximation methods which can save remarkable computational costs. The proposed frame can be used in optimization procedures for developing quieter saw blades and other rotating discs. Furthermore, the paper discusses mode splitting which is a well-known phenomenon for rotating machinery. For this, the results of sound radiation are investigated with respect to the question whether mode splitting is actually audible.

1. Introduction

Circular spinning discs are extensively used in many fields of engineering industry, e.g. computer hard drive discs, mechanical rotors, tools, and aerospace engine components. Owing to a variety of effects associated with rotation, e.g. gyroscopic effects, the dynamic behavior of such mechanical systems is still an interesting and challenging research field. The major concern of engineers when dealing with rotating structures consists in the possibility of unstable dynamic behavior which can lead to excessive deflections and thus, may cause mechanical failure or even dangerous situations for workers in the vicinity of these machines. An unstable situation, considered by the authors, arises when the excitation frequency of a spinning blade approaches the frequencies of natural modes. In this case, the force excitation gets into resonance with the mechanical system and therefore,

* Corresponding author. Technical University of Munich, 80333, Munich, Germany.
E-mail address: Marcus.Maeder@tum.de (M. Maeder).

https://doi.org/10.1016/j.jsv.2019.115085

can lead to excessive deformation if the system is weakly damped. Usually, this case becomes relevant for spinning blades made of metal or similar monolithic materials [1].

If no rotation is present, the natural modes are constant with respect to frequency as long as the mass, damping and stiffness properties remain unchanged. If rotation is considered, several effects influence the mechanical behavior [2]. On the one hand, centrifugal forces induce in-plane stresses causing additional stiffness contributions. Therefore, natural frequencies tend to rise with increasing rotation [3–5]. On the other hand, gyroscopic effects that result from a change of the radial distance of any given material particle with respect to the axis of rotation due to structural vibration, result in an unsymmetrical contribution to the mechanical behavior. As seen from a stationary observer, this effect leads to traveling waves in and against the direction of rotation. These two waves are known as forward and backward traveling waves [1]. In terms of natural modes, this effect is known as mode splitting, where the associated eigenfrequency of the backward traveling wave decreases and the eigenfrequency of the forward traveling wave increases with increasing rotational speed. Bearing this in mind, it is obvious that a critical rotational speed exists where the frequency of the backward traveling wave tends to zero. In this case, as seen from a stationary observer, the deformation is quasi static while the disc is still spinning [1,6]. In order to improve the stability of rotating discs, pretensioning or prestresses can be applied through plastic deformation [7–12].

It must be noted that the acoustic radiation of discs and plates have been discussed in literature for rotating structures [1,13–16] and for cases without rotation [14,17–21], where it is possible to derive analytical formulations [16,19,21]. The research associated with understanding noise radiation of rotating structures is often concerned with noise exposure measures that are linked to health issues of workers in the vicinity of such rotors.

In the frame of product development, computer aided engineering (CAE) is a common tool for analyzing designs in an early stage of the development process. There, the finite element method (FEM), the boundary element method (BEM) and others have proved to be suitable and reliable tools [12,14,18,22–27] for vibroacoustic analysis. In order to include sound radiation analysis in the CAE frame, efficient numerical tools need to be developed and validated. Especially in cases for which an optimization procedure is part of the development process, fast and reliable methods are necessary [24,25].

The analysis of sound radiation from vibrating structures requires to couple structure and fluid. Usually, one of two coupling strategies is applied. The first one assumes structural vibrations in vacuo which are used as boundary conditions for the fluid, see for example [17,24–26]. Hence, the structure excites the fluid but there is no feedback from the fluid to the structure. In what follows, this approach will be referred to as the one-way fluid structure interaction (FSI) approach. In literature, this approach is often called *weak coupling* or even uncoupled. The second category includes the feedback from the fluid to the structure [22,28–30]. This will be referred to as a two-way FSI approach. Synonyms will be *strong coupling* or fully coupled FSI. The proper choice of the FSI approach depends on the particular problem and needs to be chosen carefully [31,32]. Furthermore, implementing stable algorithms is not straightforward and can lead to various difficulties [33,34].

Another aspect of wave propagation is concerned with the so-called far field approximation, when dealing with exterior acoustic domains [27]. Since computing wave propagation to infinity is neither reasonable nor even possible, the computational domain must be truncated. This artificial boundary must resolve the far field conditions in order to model the physical behavior of the real system. One possible solution beside using perfectly matched layers (PML) [35–37] or absorbing boundary conditions (ABC) [38,39] consists in the use of infinite finite elements [40,41]. The boundary element method does not require a truncation of the domain since only the radiating surface appears in the simulation model [27,42].

With these methods, it is possible to compute the radiated sound power of the structure. However, the radiated sound power accounts for a global measure for assessment of the acoustic performance [43]. Therefore and owing to the costly frequency sweep, solution of the fully coupled problem for large-scale applications still requires enormous computational resources, not to speak of uncertainty quantification and optimization and even though there is a large body of scientific work on this. For this reason, approximation methods have been developed to reduce the computational costs while conserving an appropriate accuracy of the numerical results. A very simple approximation technique assumes a unit radiation efficiency, see for example [26]. The resulting radiated sound power approximation is known as Equivalent Radiated Power (ERP) which is a very simple approach usually overestimating the actual value. It can be understood as a postprocessing of a structural analysis. Another common approximation is based on a TAILOR expansion of the free field GREEN's function of the RAYLEIGH integral. It is known as the lumped parameter model (LPM) allowing to estimate the radiated sound power based just on structural analysis, too. Other than ERP, LPM is able to capture acoustic short circuit effects. For further details, the authors refer to the literature [24,26,44–46].

In this paper, the authors investigate the sound radiation from rotating discs. Results for the radiated sound power show that under certain valid simplifications, it is possible to reduce the numerical effort significantly. As an approximation, the LPM shows good agreement with respect to full finite and boundary element models. Further, the paper will compare results of one-way and fully coupled FSI.

With respect to physics, the sound radiation of mode splitting will be discussed. While the mode splitting is a well-known and well-studied effect for spinning discs, the authors have not found any clear indication in literature about whether or not the mode splitting is indeed audible. Since mode splitting is only visible for a stationary global observer, but not for the observer traveling on the rotating disk, the authors try to illuminate this problem. Indeed, the former one is more of practical interest, since a co-rotating listener is not meaningful in this sense.

The paper at hand is structured as follows: Section 2 presents a brief overview of the basic theory. Aspects such as the general model, numerical methods as well as ERP and LPM are explained. In Section 3, the simulation models and simulations are discussed. The results follow in Section 4. Some conclusions will be provided in Section 5.

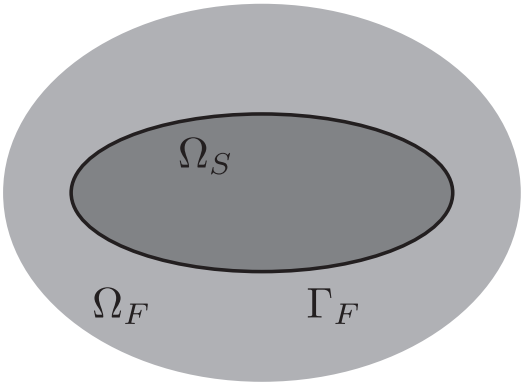

Fig. 1. Description of domain with the solid domain Ω_S and its boundary Γ_F which is surrounded by a fluid Ω_F.

2. Theoretical background

For a general description, the authors consider a three dimensional Euclidean space in $\Omega_S \subset \mathbb{R}^3$ which is bounded by a closed surface $\Gamma_F \subset \mathbb{R}^2$ that serves as a common boundary to the surrounding fluid $\Omega_F \subset \mathbb{R}^3$ which is assumed to be unbounded, cf. Fig. 1.

2.1. Numerical methods

Following the principles of the finite element method for structural dynamic problems, one can state the system of discrete equations for the structural component as [47–49]

$$\mathbf{M}\ddot{\mathbf{u}} + \mathbf{D}\dot{\mathbf{u}} + \Omega\mathbf{G}\dot{\mathbf{u}} + \mathbf{K}\mathbf{u} = \mathbf{f} \tag{1}$$

with **M**, **D**, and **K** as mass, damping, and stiffness matrices, respectively. The vector of unknowns is $\mathbf{u}(x,t)$, i.e. the nodal displacements, while the components of external nodal forces are accommodated in $\mathbf{f}(x,t)$. Further, Ω denotes the angular velocity about the axis of rotation which introduces centrifugal and gyroscopic forces that are considered by the gyroscopic matrix **G**. Typically, the gyroscopic matrix is skew symmetric if a single axis of rotation is considered only. For the remainder of this paper, a harmonic time dependence is assumed for all unknowns and excitation forces.

Equation (1) is transformed such that

$$\left[\mathbf{K} - \mathrm{j}\omega\mathbf{D} - \mathrm{j}\omega\Omega\mathbf{G} - \omega^2\mathbf{M}\right]\mathbf{U} = \mathbf{A}_s\mathbf{U} = \mathbf{F}, \tag{2}$$

where ω denotes the angular frequency and $\mathbf{A}_s$ will be referred to as dynamic stiffness matrix of the structure.

A similar approach is conducted for deriving the system matrices of the surrounding inviscid fluid. This system is given by Refs. [27,43]

$$\mathbf{A}_f(\omega)\mathbf{P}(\omega) = \mathbf{F}_f(\omega) = \mathbf{B}\mathbf{V}_f(\omega) \tag{3}$$

where $\mathbf{A}_f$ denotes the fluid system matrix and **P** the column matrix of unknown sound pressure. $\mathbf{F}_f$ contains the external forces acting on the fluid. The latter can be expressed by a matrix **B** and the fluid particle velocity $\mathbf{V}_f$. This form of formulation is achieved for both, the FEM and the BEM. For further details, the authors refer to Refs. [27,43].

2.2. Fluid structure interaction

Over the last decades, numerous methods have been developed to solve problems with fluid structure interaction, cf. [22,28,33]. For a deeper insight, the authors refer to the literature [27,34,43,50–52].

As already discussed in the introduction, two ways of coupling are considered. The first one is named one-way interaction, meaning that the continuity of the particle velocity is enforced and the second one is named two-way or full interaction, for which continuity of the particle velocity and the force equilibrium are enforced.

The first one assumes structural analysis in vacuo and its results are applied as boundary conditions to the fluid domain. The second coupling takes the full interaction of both domains into account which includes the feedback of the fluid to the structure.

Looking at the resulting system of equations

$$\begin{bmatrix} \mathbf{A}_s & \mathbf{C}_{sf} \\ \mathbf{C}_{fs} & \mathbf{A}_f \end{bmatrix} \begin{bmatrix} \mathbf{U} \\ \mathbf{P} \end{bmatrix} = \begin{bmatrix} \mathbf{F} \\ \mathbf{B}\mathbf{V}_f \end{bmatrix}, \tag{4}$$

one can identify the previously presented system of equations for the structural and the fluid domain, which are linked by the coupling matrices $\mathbf{C}_{sf}$ and $\mathbf{C}_{fs}$.

In case of one-way coupling, matrix $\mathbf{C}_{sf} = \mathbf{0}$. Then, NEUMANN boundary conditions for the fluid apply, i.e.

$$\mathbf{V}_f - \mathbf{V}_s = 0, \tag{5}$$

where $\mathbf{V}_s$ is the structural surface normal velocity, which results from an adequate structural dynamic simulation.

2.3. Simplified sound power evaluation

For most practical cases, it is necessary to solve a boundary value problem for accurate sound power evaluation even in case of a one-way coupling. Both, the FEM and the BEM are computationally expensive, in particular if frequency sweeps are considered [43]. Analytical solutions are available for a limited number of cases only, cf. [17,18,42]. To efficiently estimate the radiated sound power based on finite element analysis (FEA) simulations of the structure only, two formulations are utilized. These are the equivalent radiated power (ERP) and the lumped parameter model (LPM), respectively. Both techniques have been successfully applied for harmonic FEA, cf. [24,26].

The equivalent radiated sound power P_{ERP} is calculated as [24,26]

$$P_{ERP} = \frac{1}{2}\rho_f\, c_f \int_{\Gamma_F} |\boldsymbol{v}_n|^2 \mathrm{d}\Gamma_F. \tag{6}$$

The integral is computed over the structural surface Γ_F with the fluid mass density ρ_f, the speed of sound c_f and the normal component of the structural particle velocity $v_n = \vec{v} \cdot \vec{n}$. For the discretized finite element model, the integral is computed as the sum over N_e surface elements with the corresponding area A_μ

$$P_{ERP} = \frac{1}{2}\rho_f\, c_f \sum_{\mu=1}^{N_e} A_\mu v_{n_\mu} v_{n_\mu}^* \tag{7}$$

where the superscript $*$ represents the complex conjugated. The particle velocity on the elements is assumed to be constant which is a reasonable simplification since the structural meshes in use will be rather fine. The equivalent radiated sound power is based on the assumption of a unit radiation efficiency, i.e. $\sigma = 1$. Local effects such as acoustic short circuits between sources are neglected. Therefore, P_{ERP} is usually overestimating the radiated sound power, especially in the low frequency range.

Often, more accurate results are possible using the LPM [26]. The LPM is based on discretizing the RAYLEIGH-Integral with a TAYLOR series of the GREEN's function and constant particle velocity on the elements [15,44,45]. This formulation can be written as a double sum over all surface elements as

$$P_{LPM} = -\frac{1}{2} k\, \rho_f\, c_f \sum_{\mu=1}^{N_e} \sum_{\nu=1}^{N_e} A_\mu A_\nu \mathfrak{I}\left\{G_{\mu\nu}\right\} \mathfrak{R}\left\{v_{n_\mu} v_{n_\nu}^*\right\} \tag{8}$$

$$\text{with} \qquad \mathfrak{I}\left\{G_{\mu\nu}\right\} = -\frac{\sin(k|x_\mu - x_\nu|)}{2\pi|x_\mu - x_\nu|},$$

where k denotes the wave number and $\mathfrak{R}\{\}$ and $\mathfrak{I}\{\}$ are the real and the imaginary parts of a complex value, respectively. Since the imaginary part of the GREEN's function accounts for the interaction between sources, the use of the LPM is often a very good approximation in the low and mid frequency range, even in (some) cases for which the assumptions of a planar radiator are violated [26].

All computed results of the sound power are converted into sound power levels using common standards where $L_W = 0$ dB has a reference sound power of $P_0 = 10^{-12}$ W. For the post-processing algorithms, user defined scripts have been developed in Python language using NumPy and SciPy routines [48,53,54].

3. Simulation

Starting with the definition of the general geometry, the numerical models are presented. They have been created using Abaqus 6.14–2 CAE and calculated by the Abaqus standard solver [48]. Two different structural models are considered. The first one is a fine resolution model to verify the implemented ERP and LPM routine. The second model is a coarse model that is utilized to create solutions when rotation is applied to the structure. The reason for this approach is to keep the computational costs at a reasonable level while the effects under investigation are still recognizable. In order to verify the acoustic sound power estimates by the ERP and LPM, an adequate acoustic volume mesh and an equivalent boundary element model were created, respectively. A closer insight will be given in the dedicated sections hereafter.

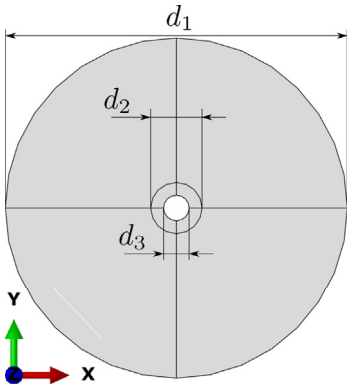

Fig. 2. Disc geometry; $d_1 = 800$ mm, $d_2 = 120$ mm, $d_3 = 60$ mm, disc thickness $t = 3.5$ mm.

Table 1
List of material properties.

Material	Property	Symbol	Value	Unit
Steel	Density	ρ_S	7800	kgm^{-3}
	E-Modulus	E	$2.1 \cdot 10^5$	MPa
	Poisson ratio	ν	0.3	–
	Damping factors	α	0.1826	s^{-1}
		β	$5.0125 \cdot 10^{-6}$	s
Air	Density	ρ_F	1.225	kgm^{-3}
	Bulk-Modulus	K	$1.42 \cdot 10^5$	Pa
	Speed of sound	c	340	m/s

3.1. Geometry and material properties

The geometry of interest - named as disc hereafter - consists of a plate structure depicted in Fig. 2, where the outer diameter d_1 and the inner diameter d_3 together with the disc thickness t define its geometrical shape. The additional diameter d_2 defines the area where a fixed-fixed boundary condition will be applied during the studies. The disc itself will be enclosed by air at rest. The disc is made of steel where HOOKE's law is considered as the linear elastic behavior for the material model. Furthermore, RAYLEIGH damping is assumed with the associated damping factors α and β. These values are set such that the critical damping ratios η_1 and η_2 of the first and second eigenfrequencies ω_1 and ω_2 take the values $\eta_1 = 1 \cdot 10^{-3}$ and $\eta_2 = 2 \cdot 10^{-3}$. Table 1 lists all the material properties.

3.2. Numerical models

Based on the created geometry, the Abaqus 6.14–2 CAE mesher is used to generate the finite element (FE) meshes. These meshes will serve as a basis for the associated boundary element models that will be analyzed with the in house BEM code *Akusta* [27,55]. In order to make the mesh data created by Abaqus available to the *Akusta* solver, a python interface routine was created.

Table 2 shows a comprehensive collection of the finite and boundary elements that where used during the simulations. Further details will be given in the subsequent sections. For a more detailed description of the Abaqus elements, the authors refer to the Abaqus documentation [48]. Constant boundary elements and their performance have been discussed in the literature [27,43].

Table 2
List of mesh properties; NoN: Number of nodes per element; Hex: 3D Hexahedral element; Tet: 3D Tetrahedral element; Quad: 2D quadrilateral element; Tri: 2D Triangular element.

Method	Domain	Software	Element type	Basis order	NoN
FEM	3D Structure	Abaqus	Hex C3D20R	quadratic	20
	3D Fluid	Abaqus	Tet AC3D10	quadratic	10
	2D Fluid	Abaqus	Tri ACIN3D6	quadratic	6
BEM	2D Fluid	Akusta	Quad	constant	1

3.2.1. Structural mesh

In order to verify the implemented ERP and LPM routines, a fine mesh resolution is chosen. Fig. 3 shows the finite element mesh for the reference model. To create this mesh, a global seeding size of 5 mm was applied. This results in a mesh of $n_{el} = 36208$ elements or with respect to the highest mode computed, approximately 40 quadratic elements per wave length of the associated mode shape. The reason for choosing such a fine mesh is due to the fact that no distorted elements are present with respect to the default aspect ratio criteria defined by the Abaqus software. For more details, the authors refer to the Abaqus documentation [48] and to Langer et al. [56]. We will present results of a brief mesh study in the subsequent section to show the applicability of the used mesh.

For further studies, it is useful to run simulations on smaller models to investigate global effects such as the mode splitting due to rotation while the computational efforts remain in reasonable expenditure. Therefore, a coarse mesh is created for fast preliminary investigations. For this coarse configuration, a global mesh seed size of $h = 20$ mm is used which, after meshing, results in a number of elements of $n_{el} = 2268$. In both cases, the symmetry plane is located at $Z = 0$.

3.2.2. Acoustic mesh

In order to quantify the feedback effect of the fluid onto the structure, a fully coupled finite element model of the surrounding fluid domain in the form of a sphere with a radius of $r = 1.5$ m is generated using three dimensional ten node tetrahedral elements, cf. Fig. 4. Here, the fluid sphere has been reduced by the volume of the disc to guarantee that the surface of the disc is shared by the structure and the fluid and no elements are overlapping or interfering with each other. Two different seeding sizes have been used for meshing. For the shared surface, the seeding size of the fluid domain was chosen as $h = 0.075$ m and on the outer boundary as $h = 0.2$ m to ensure a smooth transition from a fine mesh at the contact area between fluid and structure and a coarser mesh further away from the center of the fluid domain.

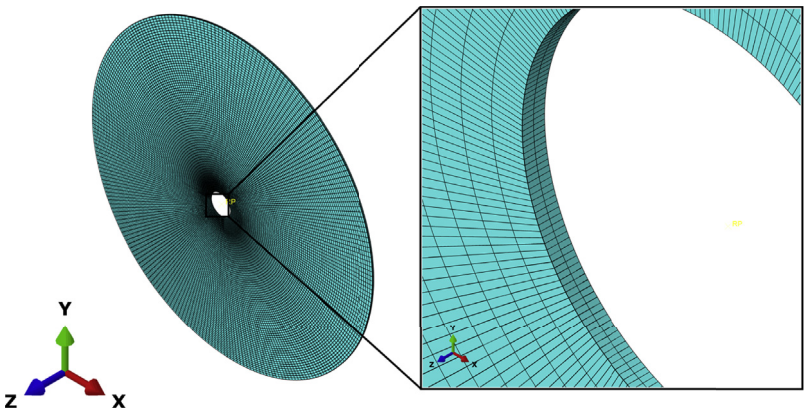

Fig. 3. Fine volumetric mesh of disc; global seeding size $h = 5$ mm, number of elements $N_e = 36208$.

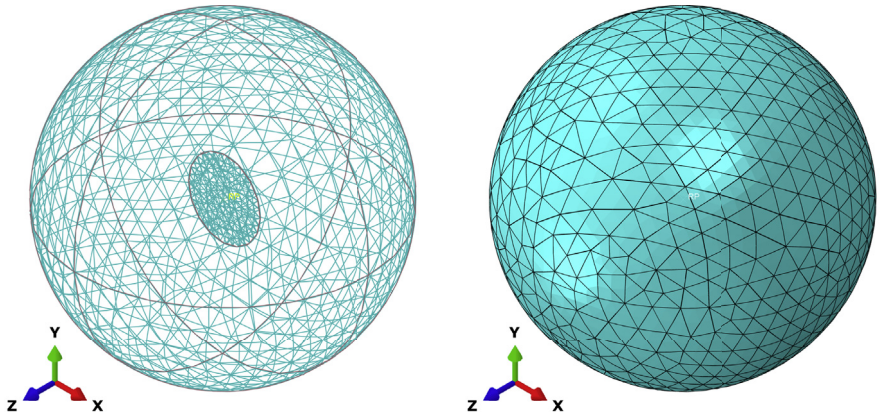

(a) Transparent 3D mesh, $h = 0.2$ m; Region of FSI seeded with $h = 0.075$ m

(b) Spherical surface meshed with infinite elements

Fig. 4. Volumetric mesh of the acoustic full space; sphere radius $r = 1.5$ m.

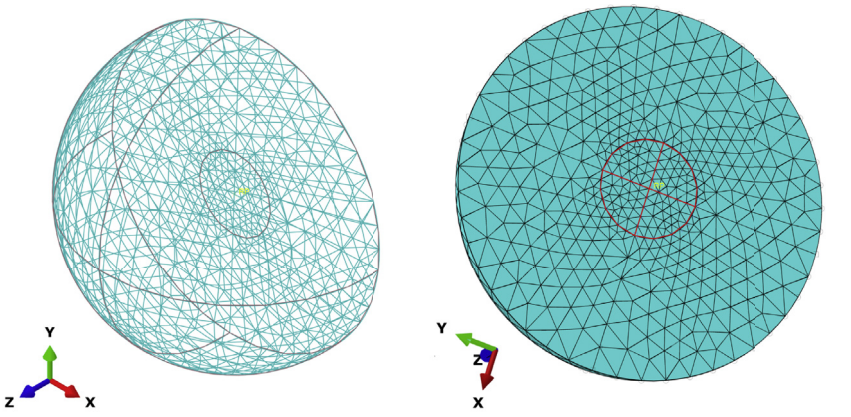

(a) Transparent 3D mesh, $h = 0.2\,\mathrm{m}$; sphere surface meshed with infinite elements

(b) Region of FSI; seeded with $h = 0.075\,\mathrm{m}$

Fig. 5. Volumetric mesh of the acoustic half space; sphere radius $r = 1.5$ m.

Since the computational effort is proportional to the size of the model, the fluid domain must be truncated at some extend. To account for the far field radiation, two dimensional infinite finite elements - called infinite elements hereafter - are attached to the outer boundary of the spherical fluid domain. These elements serve as an appropriate far field approximation. A substantial drawback with respect to the computational cost is associated with the use of infinite elements as they are implemented in Abaqus 6.14–2. The drawback lies in the fact that when using infinite elements, no modal decomposition procedure is possible, i.e. when investigating the harmonic behavior, the complete system matrix must be inverted for each frequency step. This results in large computational costs and is therefore only applicable for a limited model size when using conventional workstation machines.

To reduce the computational effort, symmetry is assumed together with appropriate boundary conditions on the symmetry plane. To take this into account, a half space model is generated, cf. Fig. 5. This is equivalent of considering a baffled plate. Here, the symmetry plane at $Z = 0$ is used to cut the acoustic domain, where symmetry boundary conditions must be applied. This topic is addressed in the subsequent sections.

3.2.3. Boundary element model

Based on the structural meshes, equivalent boundary element models are created by identifying the surface element faces of the three dimensional meshes in the positive half plane, i.e. $Z \geq 0$, and converting these faces into surface elements using a scripting interface written in Python language, cf. Fig. 6. The transferred data consists of all surface element nodes with their coordinates, the element coincidence matrix and the surface normal velocities which are the result of a preceding harmonic analysis of the structure in the frequency range of interest. Since the boundary element matrices are fully populated and thus, quite large, the authors use half space models only. This approach is justified by the assumptions for using the lumped parameter model.

3.2.4. Boundary conditions

In the following, the applied boundary conditions will be discussed. In order to tie the disc in space, two areas, i.e. front and back, of the disc defined by the geometrical parameters d_2 and d_3 are used to apply fixed-fixed boundary conditions (BC), cf. Fig. 7.

In Fig. 7(b), the Abaqus specific symbols indicate that all translational and rotational degrees of freedom are fixed. The boundary conditions are applied to surfaces. In the case of the half space radiation problem, symmetry boundary conditions are fulfilled if the velocity normal to the symmetry plane vanishes. This automatically applies to all free edges or surfaces. Therefore, no special care of the symmetry plane must be taken.

The boundary conditions for the fluid models stem from a preceding harmonic analysis of the structure. For each element which is shared by the structure and the fluid, the surface normal velocity is calculated. This information serves as the input data for the fluid model assuming a sound hard boundary conditions.

3.2.5. Excitation

For analyzing the structural behavior in frequency domain, a harmonic force excitation is considered, cf. Fig. 8. For all dynamic analysis hereafter, this force is set to $F(X = 0.4\,\mathrm{m}, Y = 0\,\mathrm{m}, Z = 0\,\mathrm{m}) = 1\,\mathrm{N}$ for all frequencies of interest and is acting in

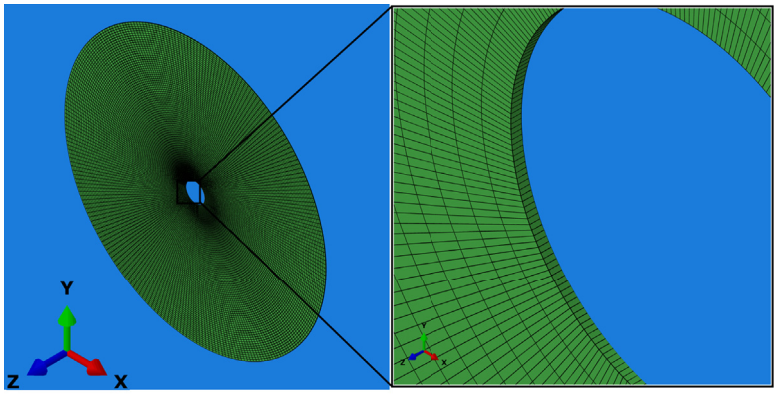

(a) Fine BEM mesh

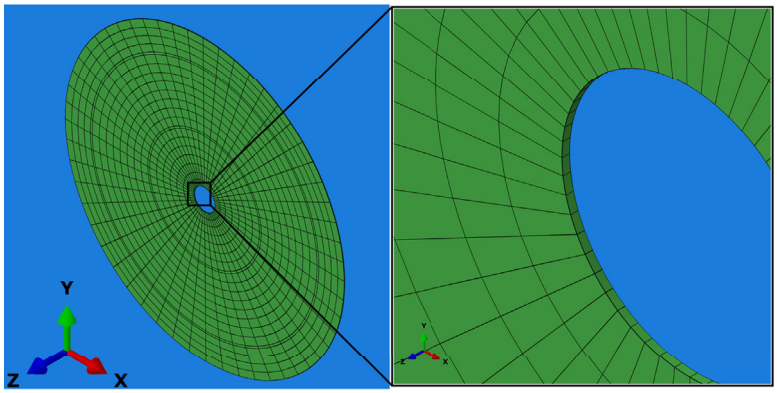

(b) Coarse BEM mesh

Fig. 6. Boundary elements in green and symmetry plane in blue color. (For interpretation of the references to color in this figure legend, the reader is referred to the Web version of this article.)

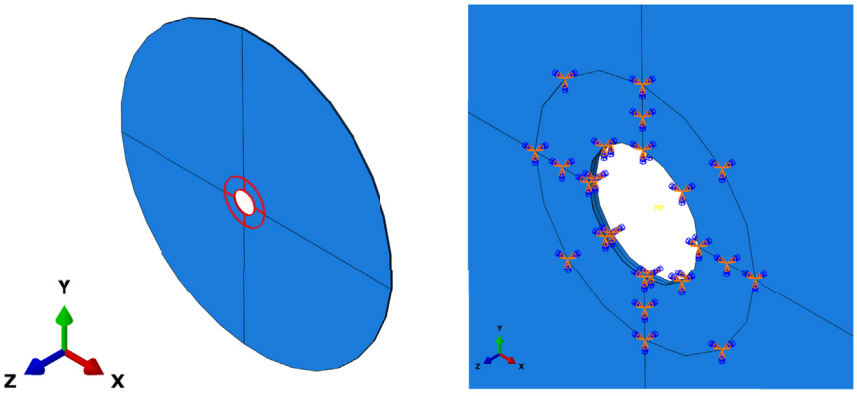

(a) Region for BC (b) Fixed-fixed BC

Fig. 7. Application of boundary conditions.

Z-direction, i.e. normal to the main discs' surface. This kind of unit force excitation is idealized and the subsequent results can be understood as transfer functions.

This force excitation has been selected to excite the out-of-plane modes of the structure since they contribute to the main sound radiation. It must be noted that for the real case, two additional forces, one in radial and one in tangential directions,

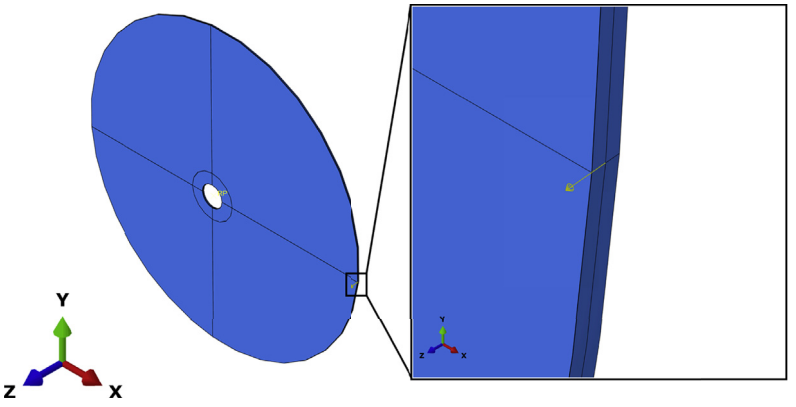

Fig. 8. Structural excitation of disc.

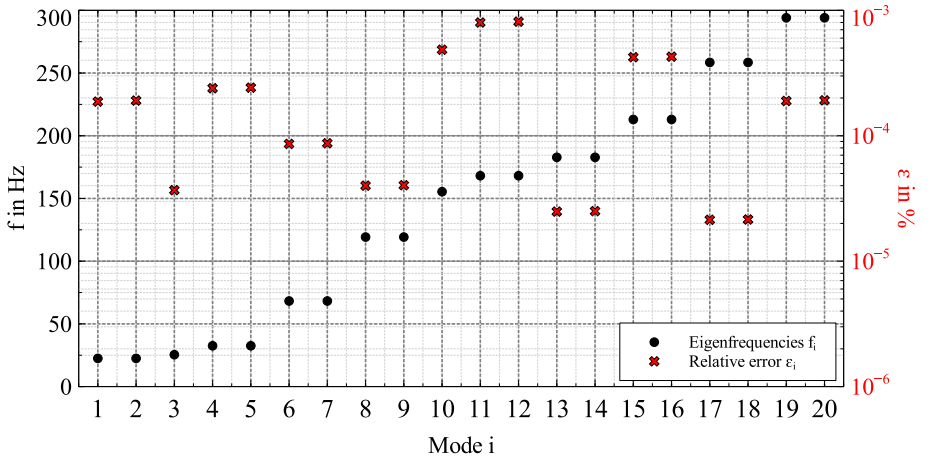

Fig. 9. Results of modal analysis and relative errors.

would act on the structure with possible excitation of in-plane modes. These modes can interact with the out-of-plane modes if the associated frequencies are close to each other. In this case, a mode coupling is possible. Preliminary studies have shown that these modes appear at frequencies above 500 Hz, which are much higher than the scope of this work and are therefore omitted. In addition, the three dimensional elastic behavior of the structure, related to the Poisson's ratio, results in an out-of-plane movement whenever an in-plane deformation is excited. Since the plate can be seen as a thin-walled structure, these out-of-plane deformations are negligible. Further, having a closer look at a realistic application such as a saw blade, it is clear that the saw teeth are not symmetrically aligned with the main geometry. Therefore, any radial or tangential force will furnish a contribution to the excitation of the out-of-plane modes. Thus, it is justified to focus on the normal plane excitation.

4. Results

In the subsequent section, the numerical results are presented and discussed. It will be shown that the numerical analysis using LPM as the acoustic radiation model is capable to correctly estimate the radiated sound power of a spinning disc while using modal superposition for harmonic analysis. All computations have been carried out on a 64 bit-Windows machine with six Intel® Xeon® CPUs E5-1650 v3 @ 3.5 GBHz cores and 64 GB B-RAM.

4.1. Modal analysis of disc

As a first step, the mesh quality is investigated comparing the results of a numerical modal analysis. For this purpose, the first 20 eigenvalues of the fine mesh configuration, cf. Fig. 3, are calculated. Taking into account the fixed-fixed boundary condition, this model results in approximately 1.8×10^6 degrees of freedom. The number of elements is 36208 and none of them is distorted when using a seeding size of $h = 5$ mm. The resulting eigenfrequencies are plotted in Fig. 9. To evaluate the accuracy of the calculations, the results of the coarse model are compared. In this model, the global seeding size was set to $h = 20$ mm, which results in 2268 elements and 26082° of freedom. 1404 elements, i.e. 61.9%, where considered as distorted in this case,

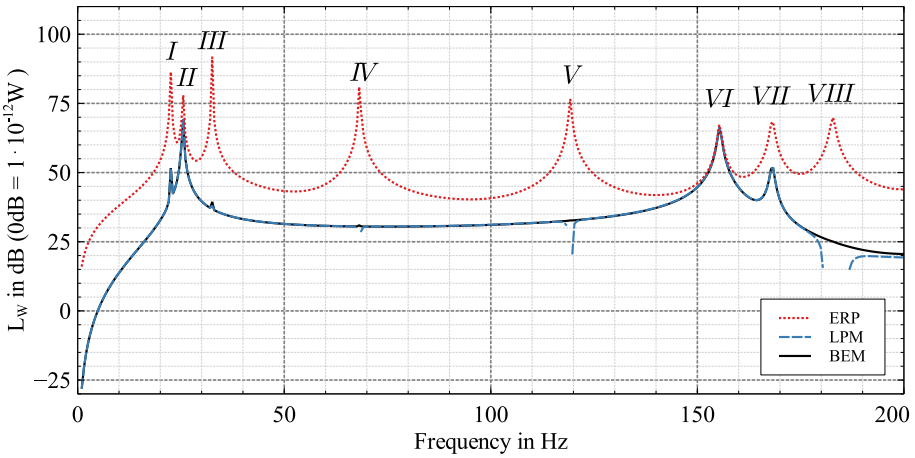

(a) Sound power level

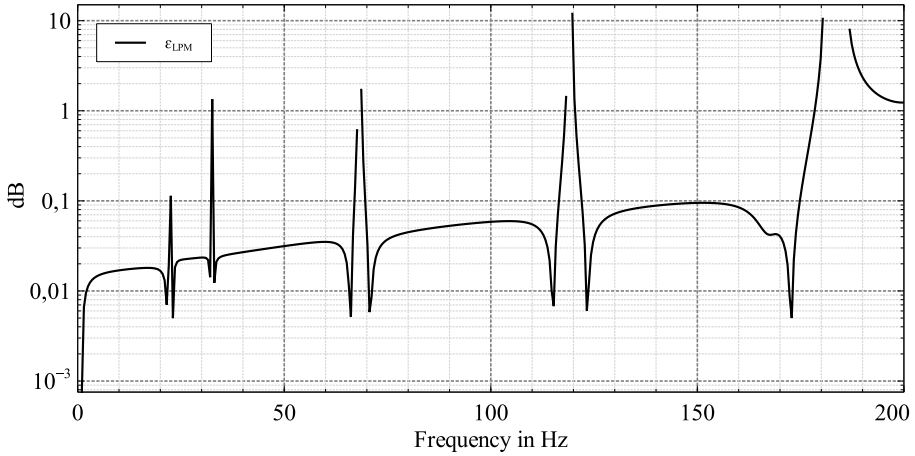

(b) Error plot between BEM and LPM results

Fig. 10. Comparison of ERP, LPM and BEM solutions; $\Omega = 0\ s^{-1}$.

which may result in inaccurate results. An error measure was calculated as follows.

$$\varepsilon_i = \frac{\left(f_{i\ fine} - f_{i\ coarse}\right)^2}{f_{i\ fine}^2}, \tag{9}$$

where *fifine* is the i-th eigenfrequency of the fine meshed model and *ficoarse* is the i-th eigenfrequency of the coarse meshed model.

It can be seen that the error values of all 20 eigenfrequencies remain below 10^{-3}. Therefore, the fine mesh model is considered as converged, cf. Langer et al. [56] for a similar discussion, and can be utilized to generate reference solutions.

4.2. Reference solutions

In this section, the fine mesh model, cf. Fig. 3, is utilized to verify the implemented routine for calculating ERP and LPM results for the non rotating case. From the theory it is known that the LPM gives exact results if the element size becomes infinitesimal small while the vibrating surface radiates sound into an acoustic half space domain under the assumption of an acoustic hard wall boundary condition on the structural surface.

To compute ERP and LPM results, the following steps were executed:

1. Compute the harmonic vibration using the fine finite element model of the structure without the acoustic domain, i.e. in vacuo.

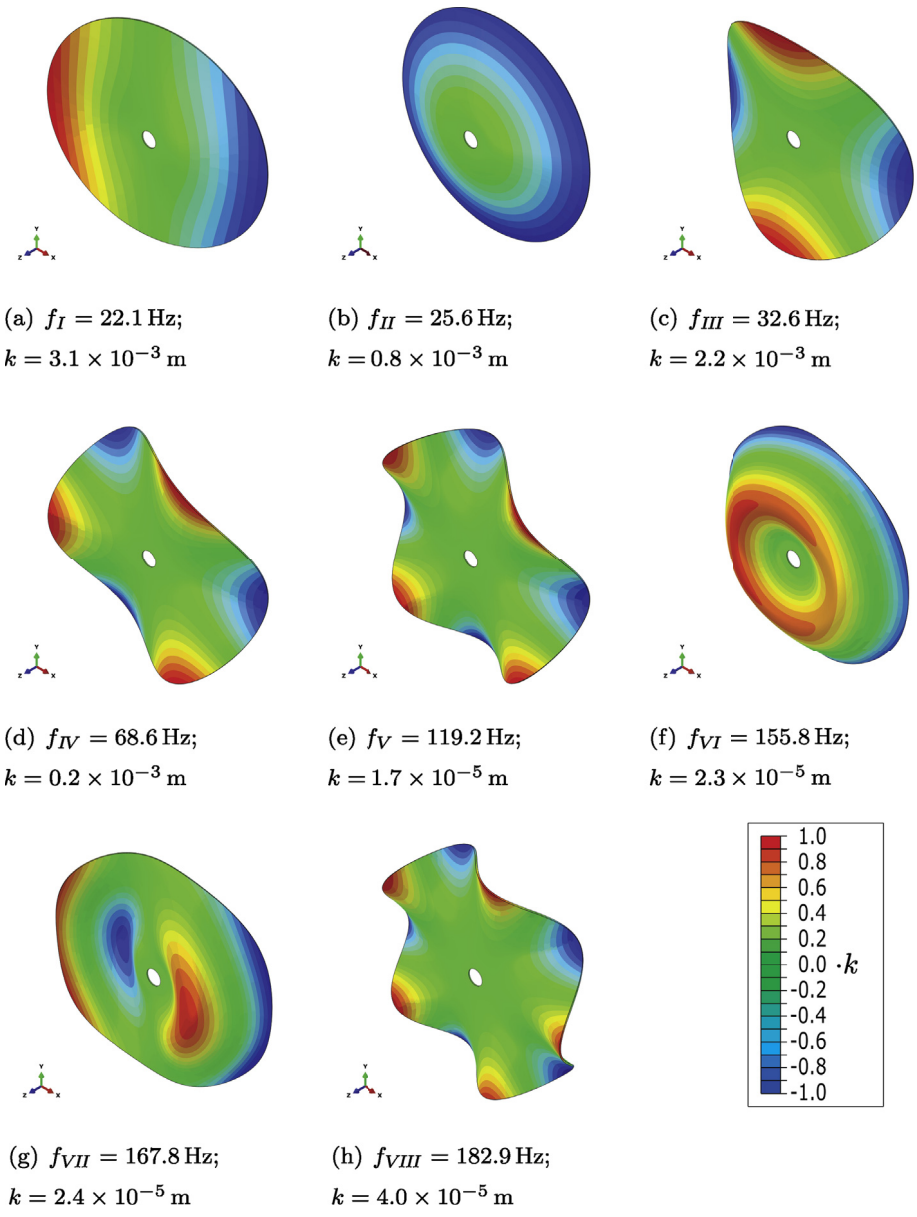

(a) $f_I = 22.1\,\text{Hz}$; $k = 3.1 \times 10^{-3}\,\text{m}$

(b) $f_{II} = 25.6\,\text{Hz}$; $k = 0.8 \times 10^{-3}\,\text{m}$

(c) $f_{III} = 32.6\,\text{Hz}$; $k = 2.2 \times 10^{-3}\,\text{m}$

(d) $f_{IV} = 68.6\,\text{Hz}$; $k = 0.2 \times 10^{-3}\,\text{m}$

(e) $f_V = 119.2\,\text{Hz}$; $k = 1.7 \times 10^{-5}\,\text{m}$

(f) $f_{VI} = 155.8\,\text{Hz}$; $k = 2.3 \times 10^{-5}\,\text{m}$

(g) $f_{VII} = 167.8\,\text{Hz}$; $k = 2.4 \times 10^{-5}\,\text{m}$

(h) $f_{VIII} = 182.9\,\text{Hz}$; $k = 4.0 \times 10^{-5}\,\text{m}$

Fig. 11. Deflection shapes at resonances, cf. Fig. 10; u_z component of deformation plotted.

2. Compute ERP and LPM results based on normal particle velocities on the structure's surface.

Similar steps are necessary to compute the reference solutions with the use of the BEM model:

1. Compute the harmonic vibration using the fine finite element model of the structure without the acoustic domain, i.e. in vacuo.
2. Transfer the surface normal velocities of the finite element model as boundary conditions into the boundary element model.
3. Calculate surface sound pressure values based on surface velocities.
4. Evaluate the sound power by integration over the whole boundary element mesh.

The results of BEM, LPM and ERP are compared in Fig. 10. Fig. 10(a) shows the sound power level whereas in Fig. 10(b), the difference between the sound power levels calculated with BEM ($L_{W_{BEM}}$) and with LPM ($L_{W_{LPM}}$), i.e.

$$\varepsilon_{LPM} = |L_{W_{BEM}} - L_{W_{LPM}}| \tag{10}$$

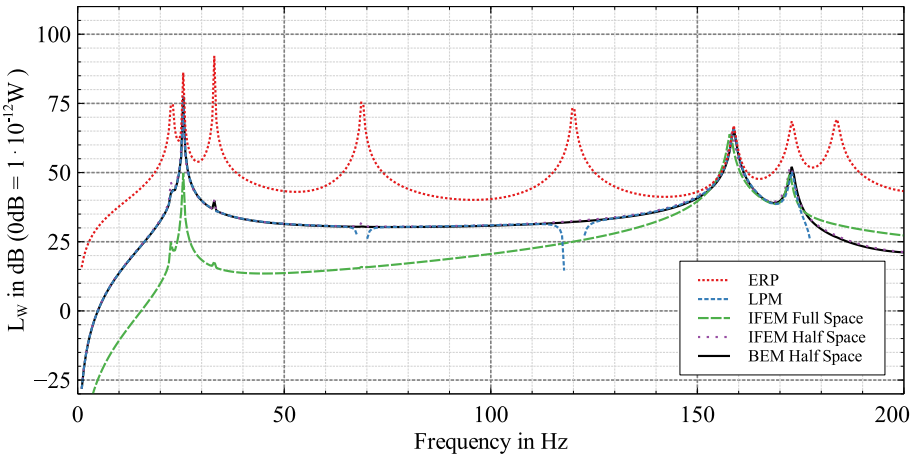

(a) $\Omega = 0\,\mathrm{s}^{-1}$

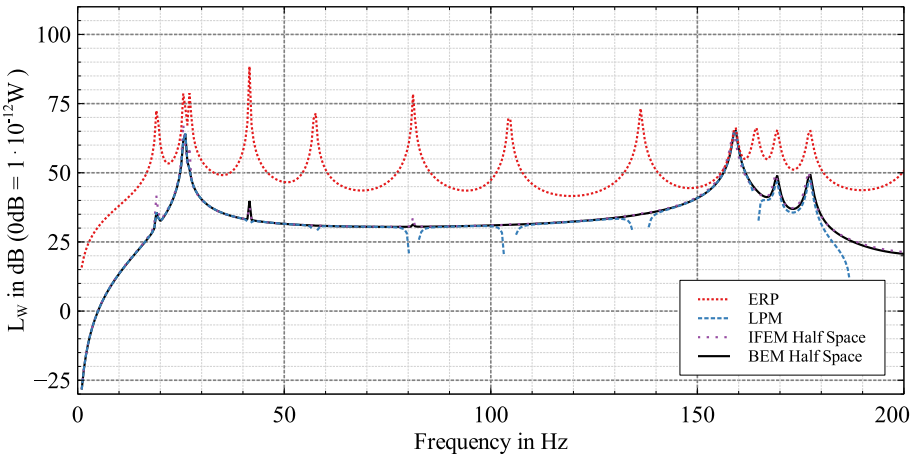

(b) $\Omega = 25\,\mathrm{s}^{-1}$

Fig. 12. Comparison of ERP, LPM, FEM and BEM solutions for coarse structural mesh.

is plotted. It can be seen that the sound power level calculated as ERP clearly overestimates the radiated sound power resulting from the boundary element model and the LPM.

Since the ERP does not consider acoustic short circuits, it is a good measure to identify structural resonances of the disc. These resonances are marked with the roman letters *I* to *VIII*, cf. Fig. 10(a). Note that such perfect acoustic short circuits require perfect symmetry. Since the kinetic energy is quite high at these resonances and technical realization of perfect symmetry quite challenging, ERP indicates at which frequencies unexpected additional resonance peaks could be observed by far-field radiation.

Further, it can be seen that the differences between the BEM and LPM results are of low level except in the vicinity of resonances where acoustic short circuits occur. The authors assume that this behavior is due to numerical errors that arise when differences of approximated values of the same size are computed as it happens for noise cancellation of acoustic short circuits. Apart from the resonances with acoustic short circuits, the LPM results match the BEM results very well. In terms of time efficiency, the wall clock times to compute the LPM and BEM results have been noted. A factor of 40–50 was identified, making the LPM computation computational more efficient. Even though the authors do not want to present an extensive computational timing analysis, the benefit in terms of saving computational resources is obvious. The reader should note that none of the in-house codes are optimized.

In Fig. 11, the u_z-component of the deflection shapes are presented. It can be seen that the sound radiation of the deflection shapes *II* and *VI* are not subjected to acoustic short circuits. *I* and *VII* produce peaks since the active vibration bulges cover large areas and are further away from each other than those of the other deflection shapes. For the remainder of this work, the numerical models are reduced in order to minimize the computational costs. It will be seen that the interesting effects are still prominent and thus can be analyzed in a more effective way.

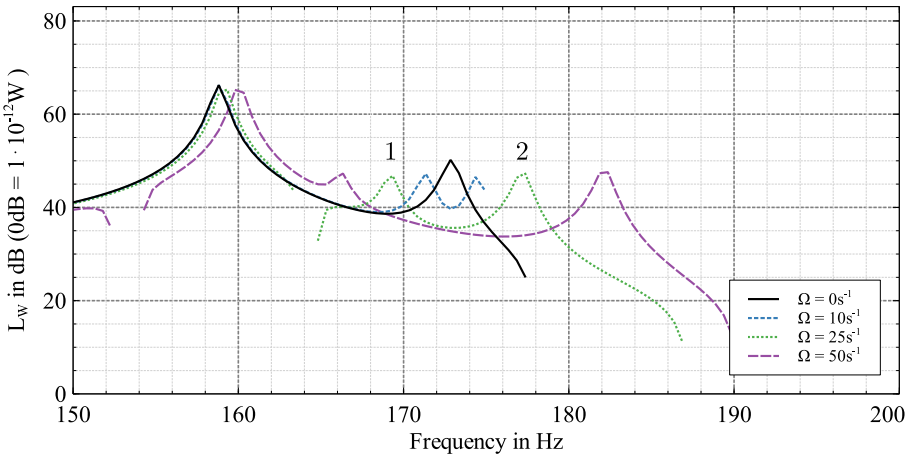

(a) Mode splitting phenomena due to an increase in rotational speed

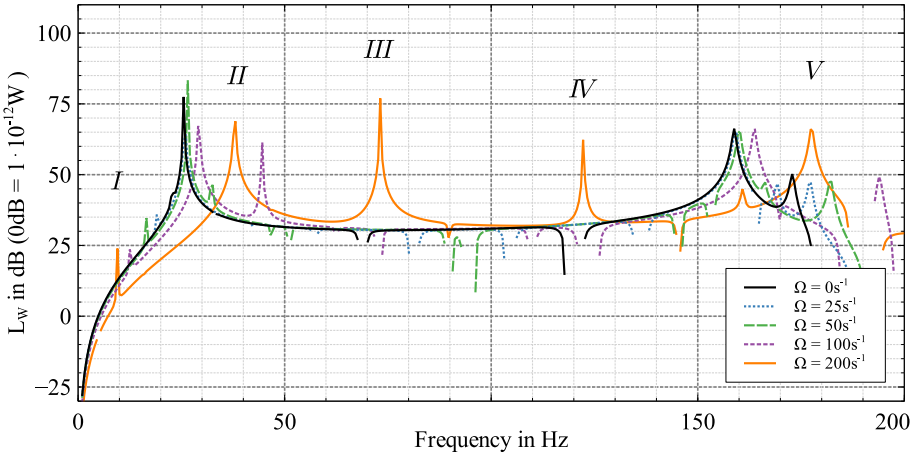

(b) Additional peaks for high rotational speeds

Fig. 13. Comparison of LPM results for different rotational speeds.

4.3. Comparing methods

In this section, the authors discuss the results computed by using different methods, namely ERP and LPM as well as the boundary element model of the half space domain, which is considered as a one-way coupled problem.

In order to study the effects of a fully coupled structure fluid interaction, two additional models are considered. The first model is a fully coupled three dimensional full space finite element model, cf. Fig. 4, and the second one is a half space approximation, cf. Fig. 5. The two fully coupled models are named “IFEM Full Space” or “IFEM Half Space”, respectively, in order to indicate that infinite elements are used as a far field approximation and the full space or half space around the disc are considered. Fig. 12 presents the results for the non-rotating case and for a rotational speed of $\Omega = 25\ \mathrm{s}^{-1}$ (or 239 rpm). Comparing the wall clock times, we can estimate a relation of timing for the non-rotating case as (t_{LPM}: t_{BEM}: $t_{FEMHalf}$: $t_{FEMFull}$) to (1: 2.5: 30: 62). Since we compare the full simulation, i.e. the time consumption of the structural dynamic analysis is included, the time relation between LPM and BEM differs with respect to the results presented in the previous section. It can be seen that the results of LPM, BEM and IFEM Half Space are in close agreement. If the full space is considered, the results show some deviations in the low frequency range where not only acoustic short circuits exist on one side of the disc but also from the front side to the backside. In addition, a slight shift of resonance peaks to lower frequencies can be noticed due to the significant mass load of the surrounding fluid. Nevertheless, it can be noted that the full space finite element model retains the same characteristics as the simplified models. Therefore, the proposed approach of simplifying the problem is assumed to be valid.

It must be noted that the proposed method is a simplification with respect to sources radiating into an acoustic half space domain. Therefore, analyzing the full space problem will not be pursued for the reminder of this paper. The readers’ attention is called when full space problems need to be analyzed.

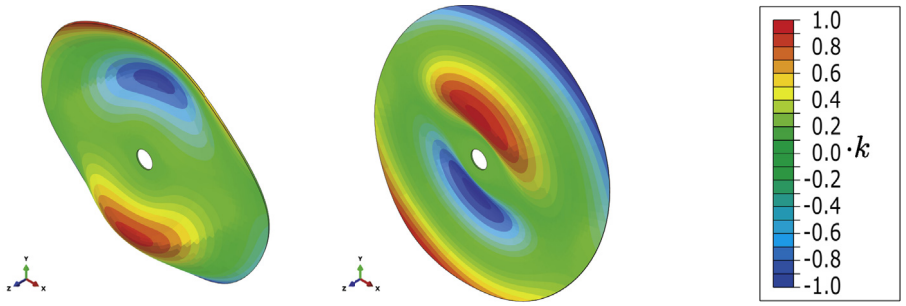

(a) $f_1 = 169.3\,\text{Hz}$; $k = 3.2 \times 10^{-5}\,\text{m}$

(b) $f_2 = 177.4\,\text{Hz}$; $k = 2.8 \times 10^{-5}\,\text{m}$

Fig. 14. Deflection shapes of resonances f_1 and f_2, cf. Fig. 13(a), for rotational speed $\Omega = 25\,\text{s}^{-1}$; u_z component of deformation plotted; $\phi = 0°$.

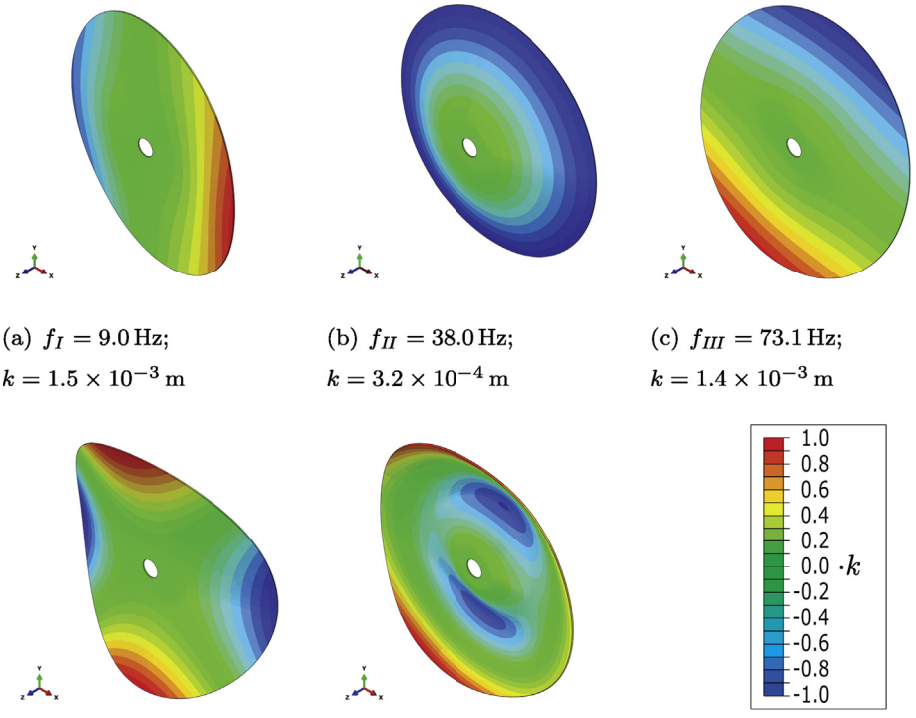

(a) $f_I = 9.0\,\text{Hz}$; $k = 1.5 \times 10^{-3}\,\text{m}$

(b) $f_{II} = 38.0\,\text{Hz}$; $k = 3.2 \times 10^{-4}\,\text{m}$

(c) $f_{III} = 73.1\,\text{Hz}$; $k = 1.4 \times 10^{-3}\,\text{m}$

(d) $f_{IV} = 122.7\,\text{Hz}$; $k = 9.7 \times 10^{-5}\,\text{m}$

(e) $f_V = 177.4\,\text{Hz}$; $k = 2.1 \times 10^{-5}\,\text{m}$

Fig. 15. Deflection shapes at resonances, cf. Fig. 13(b) with $\Omega = 200\,\text{s}^{-1}$; u_z component of deformation plotted; phase angle $\phi = 0°$.

When considering rotation of the disc, the ERP results exhibit a clear mode splitting, cf. Fig. 12(b), where, for instance, the resonance close to $f = 70$ Hz in the non-rotating case, cf. Fig. 12(a), splits up into resonances at $f = 58$ Hz and $f = 81$ Hz for the rotating case. This effect is due to superimposition of the rotational frequency and the vibrational frequency of the disc. From the outside perspective this results in a forward and backward traveling wave with respect to the rotation. Again, comparing the results of the LPM, BEM and IFEM Half Space calculations, it can be seen that all three methods give very similar results and that, in the low frequency range, acoustic short circuits can occur. Then, no resonant sound radiation is expected. Only at higher frequencies where acoustic short circuits are less pronounced due to the higher radiation efficiency, the mode splitting leads to resonant sound radiation. As a final remark, it can be stated that the LPM method can be used as a suitable numerical tool for investigating the sound radiation of rotating discs. This will be discussed in more detail in the subsequent section.

4.4. Analysis of different rotational speeds

To investigate the sound radiation from the spinning disc, different rotational speeds are considered. Fig. 13 shows results for various angular velocities Ω. It was already mentioned that for higher frequencies, acoustic short circuits are less pronounced and mode splitting can be noticed in the LPM results. Fig. 13(a) shows a zoomed window of the mentioned frequency range between $f = 150$ Hz and $f = 200$ Hz. The calculated data is plotted for $\Omega = 0\ \mathrm{s}^{-1}$, $\Omega = 10\ \mathrm{s}^{-1}$, $\Omega = 25\ \mathrm{s}^{-1}$ and $\Omega = 50\ \mathrm{s}^{-1}$. It can be clearly seen that once the rotational speed increases, the resonance peaks start to split where the resonance associated with the backward traveling wave decreases in frequency and the resonance associated with the forward traveling wave increases. This effect is not symmetric with respect to the resonance frequency of the non-rotating disc since centrifugal forces lead to an increase in stiffness of the whole system. It is clearly identified for the resonance at $f = 159$ Hz for the non-rotating case which is then shifted up to $f = 160$ Hz for the case where the rotational speed is increased to $\Omega = 50\ \mathrm{s}^{-1}$, cf. Fig. 13(a).

Exemplarily, Fig. 14 pictures the deflections shapes of the two resonances in Fig. 13(a) marked with the numbers "1" and "2" for the rotational speed of $\Omega = 25\ \mathrm{s}^{-1}$.

It can be seen that the form of the deflection shape is similar and that, at first glance, only the associated frequencies differ. The second difference that the authors want to point out is that the deflections shapes have a complex form, i.e. that the radial nodal lines of the deflection shape do not remain at their initial position but rather rotate in the opposite direction of the rotation for the backward traveling wave and rotate with the direction of the rotation for the forward traveling wave. This will be discussed in more detail later in this section.

For a wide range of rotational speeds, i.e. up to $\Omega = 50\ \mathrm{s}^{-1}$, no identifiable resonances occur between $f = 50$ Hz and $f = 150$ Hz. In contrast, when the rotational speed is increased up to $\Omega = 200\ \mathrm{s}^{-1}$, suddenly resonances occur. This is somehow surprising since the associated deflection shapes of deflection *III* and *IV*, cf. Fig. 15(c) and (d), respectively, tend to form acoustic short circuits. A possible explanation, proposed by the authors, can be related to the fact that for the rotating case, stationary nodal lines of the deflection shapes are not pronounced anymore. They rather consist of stationary and traveling wave components. Due to the traveling wave characteristics, acoustic short circuits are less likely to occur and thus resulting in additional peaks in the far field radiation spectrum. Similar discussions have been conducted in Unruh at al. [57] and Liu et al. [58].

Further, the authors present the deformations shapes of the rotating deflection shapes associated with the rotational speed of $\Omega = 200\ \mathrm{s}^{-1}$ at the resonant frequencies of $f_I = 9.0$ Hz and $f_{III} = 73.1$ Hz, cf. Figs. 13(b) and 15. Figs. 16 and 17 show the deflection shapes of the mentioned resonances for different phase angles of the vibration. It can be seen that in Fig. 16, the nodal line stretching in radial direction rotates in the opposite direction of the rotation whereas in Fig. 17, the nodal line rotates in the direction of the discs' rotation. The latter one can be regarded as acoustically relevant as long as the vibrating frequency remains in the audible frequency range. Since the associated frequency of the backward traveling wave $f_I = 9.0$ Hz is below the audible frequency range of $f = 20.0$ Hz, it can be neglected with respect to usual acoustic problems. However, from a mechanical point of view this vibration is more crucial since there exists a critical rotational speed Ω_{crit} where the associated frequency of the vibration tends to zero. This phenomenon is similar to a tumbling rotor where it is called wobbling [59]. For the case where the vibrating frequency is zero, a fixed observer recognizes a stationary deflection of the disc while still spinning.

As a final remark, the question will be addressed whether the mode splitting is audible or not. For this reason, the sound pressure is evaluated at three different positions in the YZ-plane, cf. Fig. 18, of the half space model, namely at $\Phi = 0°$, $\Phi = 45°$ and $\Phi = 90°$ according to the definition of Φ which can be found in Fig. 18(a). Fig. 18(b) depicts the real part of the sound pressure taken from the surface of the half space model, i.e. the disc is considered as baffled, plotted in the frequency range between $f = 150$ Hz and $f = 180$ Hz where the disc is rotating with $\Omega = 25\ \mathrm{s}^{-1}$. It can be seen that if a listener is located on the axis of rotation, no mode splitting is audible. When moving away from the axis of rotation, mode splitting is audible.

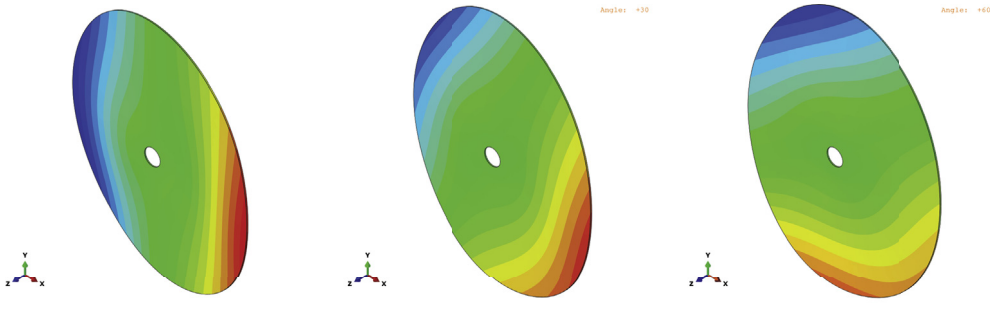

Fig. 16. Deflection shapes at phase angles at resonance f_I with $\Omega = 200\ \mathrm{s}^{-1}$; u_z component of deformation plotted.

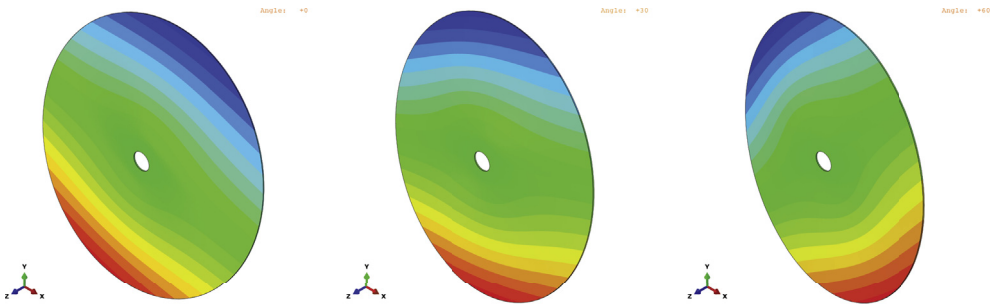

(a) $\varphi = 0°$ (b) $\varphi = 30°$ (c) $\varphi = 60°$

Fig. 17. Deflection shapes at phase angles at resonance f_{III} with $\Omega = 200\ \mathrm{s}^{-1}$; u_z component of deformation plotted.

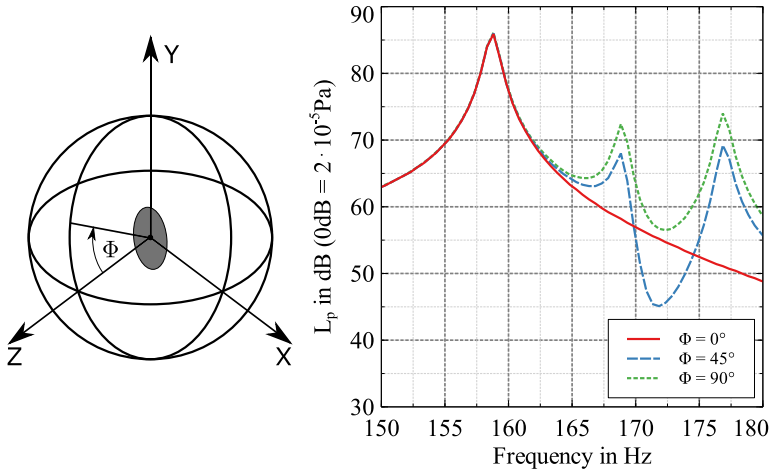

(a) Definition of Φ (b) Real part of sound pressure

Fig. 18. Sound radiation at different polar coordinates for $\Omega = 25\ \mathrm{s}^{-1}$.

5. Conclusions

In conclusion, the authors want to point out the following statements. At first, the fully coupled finite element model gives the most accurate results, where acoustic short circuits on the disc surface as well as between the front and the back side are considered. Further, the mass loading of the full space model is recognizable by means of shifts in the resonance frequencies. Second, ERP and LPM are suitable approaches for computing sound power values of rotating structures. It must be noted that the LPM assumes a baffled sound radiator. In addition, it is a valid approach to simplify the structural normal surface velocity across a finite element if the element size is adequate. Comparing results of LPM and ERP enables the user to identify acoustic short circuits. For the cases where acoustic short circuits are present, one should choose LPM over ERP. Third, utilizing LPM reduces the computational efforts by a factor of 50 compared to an equivalent BEM simulation and a factor of 60 compared to the full FEM simulation where FEA is included within the LPM timing. Fourth, for high rotational speeds, additional resonances occur. It is expected that cancellation effects due to acoustic short circuits are not present anymore. Last but not least, the authors identified that mode splitting is audible but not along the axis of rotation.

Based on these conclusions, the authors see the LPM as a useful tool to integrate sound power estimations to the frame of acoustic optimization problems of rotating structures.

Author contribution statement

Maeder, Marcus: Conceptualization, Methodology, Software, Validation, Formal analysis, Investigation, Data Curation, Writing - Original Draft, Writing - Review & Editing, Visualization, Project administration. **D' Auria, Roberto**: Methodology, Software, Investigation, Writing - Original Draft, Writing - Review & Editing. **Grasso, Ettore**: Conceptualization, Methodology, Software,

Investigation, Writing - Original Draft, Writing - Review & Editing. **Petrone, Giuseppe**: Writing - Review & Editing. **De Rosa, Sergio**: Writing - Review & Editing, Supervision. **Klaerner, Matthias**: Software, Writing - Review & Editing. **Kroll, Lothar**: Supervision. **Marburg, Steffen**: Resources, Writing - Review & Editing, Supervision.

References

[1] C.D. Mote, R. Szymani, A review report on principal developments in thin circular saw vibration and control research, Holz Roh Werkst. 35 (5) (1977) 189–196.
[2] H. Lamb, R.V. Southwell, The Vibration of a Spinning Disk, The Royal Society Publishing.
[3] W. Eversman, J.R.O. Dodson, Free vibration of a centrally clamped spinning circular disk, AIAA J. 7 (10) (1969) 2010–2012.
[4] T. Kiesel, S. Marburg, Simulation of mode-locking phenomena in a complex nonlinear rotor system using 3d solid finite elements, Proceed. Inst. Mech. Eng., Part C: J. Mech. Eng. Sci. 230 (6) (2016) 959–973, https://doi.org/10.1177/0954406215617196.
[5] S. Huang, W. Soedel, Effects of coriolis acceleration on the free and forced in-plane vibrations of rotating rings on elastic foundation, J. Sound Vib. 115 (2) (1987) 253–274.
[6] M.A. Prohl, A general method for calculating critical speeds of flexible rotors, Trans. ASME 67 (1945) A142.
[7] W. Prager, Recent developments in the mathematical theory of plasticity, J. Appl. Phys. 20 (3) (1949) 235–241.
[8] G.S. Schajer, C.D. Mote, Analysis of roll tensioning and its influence on circular saw stability, Wood Sci. Technol. 17 (4) (1983) 287–302.
[9] U. Heisel, T. Stehle, H. Ghassemi, Experimental investigation into parameters influencing roll tensioning of circular saw blades, J. Mach. Eng. 15 (2015).
[10] M. Na, R. uri, T. Nnsi, Prediction of modal properties of circular disc with pre-stressed fields, MATEC Web Conf. 157 (2018) 02034, https://doi.org/10.1051/matecconf/201815702034.
[11] M. Na, Structural dynamic modification of vibrating systems, Appl. Comput. Mech. 1 (2007) 203–214.
[12] N. Nicoletti, E. Aubry, D. Fendeleur, M. Renner, A finite element model for the analysis of roll burnishing, Holz Roh Werkst. 55 (24) (1997) 183–187.
[13] R. Chanaud, Experimental study of aerodynamic sound from a rotating disk, J. Acoust. Soc. Am. 45 (2) (1969) 392–397.
[14] L. Chen, D. Schweikert, Sound radiation from an arbitrary body, J. Acoust. Soc. Am. 35 (10) (1963) 1626–1632.
[15] G.H. Koopmann, J.B. Fahnline, Active Control of Radiated Acoustic Power, Designing Quiet Structures, Academic Press, London, 1997, pp. 179–200.
[16] M. Lee, R. Singh, Analytical formulations for annular disk sound radiation using structural modes, J. Acoust. Soc. Am. 95 (6) (1994) 3311–3323, https://doi.org/10.1121/1.409993.
[17] O. Tger, M. Dannemann, W.A. Hufenbach, Analytical study of the structural-dynamics and sound radiation of anisotropic multilayered fibre-reinforced composites, J. Sound Vib. 342 (2015) 57–74.
[18] L. Cremer, M. Heckl, B. Petersson, Structure-Borne Sound, Springer Berlin Heidelberg, 2005.
[19] H. Lee, R. Singh, Acoustic radiation from out-of-plane modes of an annular disk using thin and thick plate theories, J. Sound Vib. 282 (1) (2005) 313–339, https://doi.org/10.1016/j.jsv.2004.02.059.
[20] F. Gao, Y. Yan, F.F. Yap, Study on idle noise characteristics of hard disk drives based on a multibody dynamic formulation, Mech. Based Des. Struct. Mach. 33 (2) (2005) 215–241, https://doi.org/10.1081/SME-200067068.
[21] A. Chatterjee, V. Ranjan, M.S. Azam, M. Rao, Theoretical and numerical estimation of vibroacoustic behavior of clamped free parabolic tapered annular circular plate with different arrangement of stiffener patches, Appl. Sci. 8 (12) (2018), https://doi.org/10.3390/app8122542.
[22] H. Lee, M.C. Song, J.C. Suh, B.J. Chang, Hydro-elastic analysis of marine propellers based on a bem-fem coupled fsi algorithm, Int. J. Nav. Architect. Ocean Eng. 6 (3) (2014) 562–577.
[23] I. Harari, K. Grosh, T.J.R. Hughes, M. Malhotra, P.M. Pinsky, J.R. Stewart, L.L. Thompson, Recent developments in finite element methods for structural acoustics, Arch. Comput. Methods Eng. 3 (2) (1996) 131–309, https://doi.org/10.1007/BF03041209.
[24] M. Klaerner, M. Wuehrl, L. Kroll, S. Marburg, Fea-based methods for optimising structure-borne sound radiation, Mech. Syst. Signal Process. 89 (2017) 37–47, https://doi.org/10.1016/j.ymssp.2016.07.019.
[25] D. Fritze, S. Marburg, H. Hardtke, Reducing radiated sound power of plates and shallow shells by local modification of geometry, Acta Acustica United Acustica 89 (1) (2003) 53–60.
[26] D. Fritze, S. Marburg, H.-J. Hardtke, Estimation of radiated sound power: a case study on common approximation methods, Acta Acustica United Acustica 95 (5) (2009) 833–842.
[27] S. Marburg, B. Nolte (Eds.), Computational Acoustics of Noise Propagation in Fluids - Finite and Boundary Element Methods, Springer-Verlag, Berlin, Heidelberg, 2008.
[28] Y. Cheng, H. Zhang, Immersed boundary method and lattice Boltzmann method coupled fsi simulation of mitral leaflet flow, Comput. Fluid 39 (5) (2010) 871–881.
[29] H.G. Matthies, R. Niekamp, J. Steindorf, Algorithms for strong coupling procedures, Comput. Methods Appl. Mech. Eng. 195 (1718) (2006) 2028–2049.
[30] M. Mnsch, M. Breuer, Numerical simulation of fluidstructure interaction using eddyresolving schemes, in: Fluid Structure Interaction II, Springer, 2011, pp. 221–253.
[31] F. Benra, H. Dohmen, J. Pei, S. Schuster, B. Wan, A comparison of one-way and two-way coupling methods for numerical analysis of fluid-structure interactions, J. Appl. Math. 2011 (6) (2011) 1–16, https://doi.org/10.1155/2011/853560.
[32] Q. Zhang, T. Hisada, Studies of the strong coupling and weak coupling methods in fsi analysis, Int. J. Numer. Methods Eng. 60 (12) (2004) 2013–2029.
[33] J. Degroote, P. Bruggeman, R. Haelterman, J. Vierendeels, Stability of a coupling technique for partitioned solvers in fsi applications, Comput. Struct. 86 (2324) (2008) 2224–2234.
[34] G. Hou, J. Wang, A. Layton, Numerical methods for fluid-structure interaction - a review, Commun. Comput. Phys. 12 (2) (2012) 337–377.
[35] A. Bermdez, L. Hervella-Nieto, A. Prieto, R. Rodrguez, Perfectly matched layers for time-harmonic second order elliptic problems, Arch. Comput. Methods Eng. 17 (1) (2010) 77–107, https://doi.org/10.1007/s11831-010-9041-6.
[36] B. Kaltenbacher, M. Kaltenbacher, I. Sim, A modified and stable version of a perfectly matched layer technique for the 3-d second order wave equation in time domain with an application to aeroacoustics, J. Comput. Phys. 235 (2013) 407–422, https://doi.org/10.1016/j.jcp.2012.10.016.
[37] A. Hppe, M. Kaltenbacher, Stable matched layer for the acoustic conservation equations in the time domain, J. Comput. Acoust. 20 (01) (2012) 1250004, https://doi.org/10.1142/S0218396X11004511.
[38] D. Givoli, Computational absorbing boundaries, in: S. Marburg, B. Nolte (Eds.), Computational Acoustics of Noise Propagation in Fluids - Finite and Boundary Element Methods, Springer Berlin Heidelberg, Berlin, Heidelberg, 2008, pp. 145–166, https://doi.org/10.1007/978-3-540-77448-8_6.
[39] D. Givoli, T. Hagstrom, I. Patlashenko, Finite element formulation with high-order absorbing boundary conditions for time-dependent waves, Comput. Methods Appl. Mech. Eng. 195 (29) (2006) 3666–3690, https://doi.org/10.1016/j.cma.2005.01.021 absorbing Boundary Conditions.
[40] L. Moheit, S. Marburg, Normal modes and modal reduction in exterior acoustics, J. Theor. Comput. Acoust. 26 (03) (2018) 1850029, https://doi.org/10.1142/S2591728518500299.
[41] R. Astley, G. Macaulay, J. Coyette, Mapped wave envelope elements for acoustical radiation and scattering, J. Sound Vib. 170 (1) (1994) 97–118, https://doi.org/10.1006/jsvi.1994.1048.
[42] F.P. Mechel (Ed.), Formulas of Acoustics, second ed., Springer-Verlag, Berlin, Heidelberg, 2008.
[43] S. Marburg, Developments in structural-acoustic optimization for passive noise control, Arch. Comput. Methods Eng. 9 (4) (2002) 291–370, https://doi.org/10.1007/BF03041465.

[44] J.B. Fahnline, G.H. Koopmann, A lumped parameter model for the acoustic power output from a vibrating structure, J. Acoust. Soc. Am. 100 (6) (1996) 3539–3547.
[45] J.B. Fahnline, G.H. Koopmann, Numerical implementation of the lumped parameter model for the acoustic power output of a vibrating structure, J. Acoust. Soc. Am. 102 (1) (1997) 179–192.
[46] G.H. Koopmann, J.B. Fahnline, Designing Quiet Structures, Academic Press, London, 1997.
[47] G. Genta, Dynamics of Rotating Systems, Mechanical Engineering Series, Springer ScienceBusiness Media, Inc, New York, NY, 2005.
[48] Dassault Systmes, ABAQUS Product Documentation, Release Abaqus 6.14-2, Providence, RI, USA: Dassault Systmes 2014, 2017.
[49] Y. Liu, Y. Zhao, Z.-Q. Lang, J. Li, X. Yan, S. Zhao, Weighted contribution rate of nonlinear output frequency response functions and its application to rotor system fault diagnosis, J. Sound Vib. 460 (2019) 114882, https://doi.org/10.1016/j.jsv.2019.114882.
[50] M.S. Howe, Acoustics of Fluid-Structure Interactions, Cambridge Monographs on Mechanics, Cambridge University Press, 1998, https://doi.org/10.1017/CBO9780511662898.
[51] Y. Bazilevs, K. Takizawa, T.E. Tezduyar, Computational Fluid-Structure Interaction: Methods and Applications, Wiley Series in Computational Mechanics, Wiley, 2013. Chichester, West Sussex, United Kingdom.
[52] O.C. Zienkiewicz, R.L. Taylor, P. Nithiarasu, The Finite Element Method for Fluid Dynamics, seventh ed., Butterworth-Heinemann, Oxford and Waltham, Mass., 2014.
[53] T.E. Oliphant, A Guide to NumPy, vol. 1, Trelgol Publishing USA, 2006.
[54] T.E. Oliphant, Python for scientific computing, Comput. Sci. Eng. 9 (3) (2007) 10–20, https://doi.org/10.1109/MCSE.2007.58.
[55] S. Marburg, S. Schneider, Influence of element types on numeric error for acoustic boundary elements, J. Comput. Acoust. 11 (03) (2003) 363–386, https://doi.org/10.1142/S0218396X03001985.
[56] P. Langer, M. Maeder, C. Guist, M. Krause, S. Marburg, More than six elements per wavelength: the practical use of structural finite element models and their accuracy in comparison with experimental results, J. Comput. Acoust. 25 (04) (2017) 1750025, https://doi.org/10.1142/S0218396X17500254.
[57] O. Unruh, M. Sinapius, H.P. Monner, Sound radiation properties of complex modes in rectangular plates: a numerical study, Acta Acustica United Acustica 101 (1) (2015) 62–72, https://doi.org/10.3813/AAA.918805.
[58] D. Liu, S. Marburg, C. Geweth, N. Kessissoglou, Non-negative intensity for structures with inhomogeneous damping, J. Theor. Comput. Acoust. 27 (01) (2019) 1850050, https://doi.org/10.1142/S2591728518500500.
[59] A. Fidlin, O. Drozdetskaya, B. Waltersberger, On the minimal model for the low frequency wobbling instability of friction discs, Eur. J. Mech. A Solid. 30 (5) (2011) 665–672, https://doi.org/10.1016/j.euromechsol.2011.03.009.